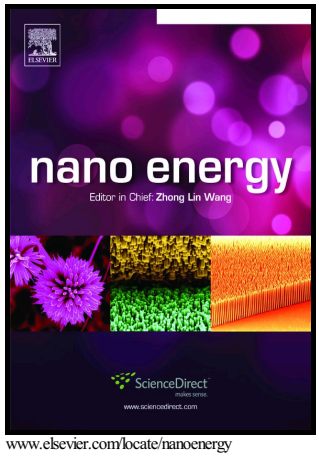

www.elsevier.com/locate/nanoenergy

Graphene Oxide-Templated Synthesis of Ternary Oxide Nanosheets for High-Performance Li-Ion Battery Anodes

Ayman A. AbdelHamid, Jun Hui Soh, Yue Yu, Jackie Y. Ying

PII: S2211-2855(17)30777-2
DOI: https://doi.org/10.1016/j.nanoen.2017.12.009
Reference: NANOEN2390

To appear in: *Nano Energy*

Received date: 16 October 2017
Revised date: 4 December 2017
Accepted date: 5 December 2017

Cite this article as: Ayman A. AbdelHamid, Jun Hui Soh, Yue Yu and Jackie Y. Ying, Graphene Oxide-Templated Synthesis of Ternary Oxide Nanosheets for High-Performance Li-Ion Battery Anodes, *Nano Energy,* https://doi.org/10.1016/j.nanoen.2017.12.009

Graphene Oxide-Templated Synthesis of Ternary Oxide Nanosheets for High-Performance Li-Ion Battery Anodes

Ayman A. AbdelHamid[a], *Jun Hui Soh*[a], *Yue Yu*[a], and *Jackie Y. Ying*[a]*

[a] *Institute of Bioengineering and Nanotechnology, 31 Biopolis Way, The Nanos, Singapore 138669*

**E-mail address*: jyying@ibn.a-star.edu.sg (J. Y. Ying)

Abstract

Ternary oxide nanosheets are very promising Li-ion battery anode materials. However, they are challenging to synthesize due to their complex compositions. Current ternary oxide nanosheet synthesis strategies are limited and not scalable. Herein, a general methodology is presented for the synthesis of ternary oxide nanosheets with controlled compositions and properties, using graphene oxide as two-dimensional template. $TiNb_2O_7$ and $Ti_{0.61}Nb_{1.29}O_4$ have been synthesized as nanosheets for the first time using the graphene oxide-templated method. In addition, $Ni_xCo_{3-x}O_4$ and $Mn_xCo_{3-x}O_4$ nanosheets have been prepared with tunable compositions. The ternary oxide nanosheets were applied as Li-ion battery anodes with very promising performance.

Keywords: Ternary oxides; nanosheets; template; graphene oxide; Li-ion batteries

1. Introduction

Ternary oxides are promising Li-ion battery (LIB) anode materials as they offer new phases with unique Li^+ storage characteristics. For example, $Li_4Ti_5O_{12}$ has been demonstrated as a safe and highly stable LIB anode with excellent rate capability [1]. Another example is $TiNb_2O_7$, which was introduced in 2011 [2] as a safe LIB anode operating at > 1 V vs. Li^+/Li. $TiNb_2O_7$ has a high theoretical specific capacity of 387.6 mAh/g, which arises from its ability to intercalate 5 Li^+ per unit formula, making use of Ti^{4+}/Ti^{3+}, Nb^{5+}/Nb^{4+} and Nb^{4+}/Nb^{3+} redox couples [3]. In addition, ternary oxides, such as $NiCo_2O_4$ and $MnCo_2O_4$, have better electrochemical and mechanical properties than binary oxides [4-7]. These ternary oxides store Li^+ by conversion reaction; hence, they are not regarded as new materials with unique Li^+ storage properties because the ternary phase decomposes during the first discharge, leading to the formation of two different binary oxides. However, it has been demonstrated that the presence of mixed oxides would improve LIB anode performance synergistically [8]. Ternary oxides can also reduce overall material cost and toxicity by partially substituting expensive and toxic metals such as Co with less expensive and more environmentally friendly metals, such as Ni and Mn [7-10].

Ternary oxide nanomaterials and nanocomposites have shown promising Li^+ storage performance. $TiNb_2O_7$ nanoparticles synthesized using SBA-15 template could retain 175 mAh/g after 300 cycles at 1C, and ~76 mAh/g at 10C [11]. Li *et al.* reported $TiNb_2O_7$ nanoparticles anchored to graphene sheets, which showed a remarkable rate performance, with a capacity of 136 mAh/g at 8C [12]. $NiCo_2O_4$/reduced graphene oxide (rGO) nanocomposite has a stable performance at 0.1 A/g, achieving 816 mAh/g after 70 cycles. It could retain 396 mAh/g at 0.8 A/g [13]. $MnCo_2O_4$ nanosheet arrays have displayed superior full-cell performance, as compared to Co_3O_4 nanosheets, mainly due to their lower average potential that resulted in higher full-cell output voltage [14]. $MnCo_2O_4$/graphene nanocomposite achieved a capacity of ~868 mAh/g after 80 cycles at 0.1 A/g [15]. Graphene incorporation could improve the performance of ternary oxides by enhancing electrode conductivity, buffering volume change and preventing contact loss [12, 13, 15].

Energy storage performance of ternary oxide could be improved by adopting the nanosheet morphology. This is due to the unique properties of the two-dimensional (2D) nanostructure that enhance the electrochemical activity and stability of the electrode [16-22]. For example, $NiCo_2O_4$ nanosheets, grown on rGO, showed very good LIB anode performance, achieving ~437 mAh/g at 1 A/g [23]. However, the synthesis of ternary oxide

nanosheets is more difficult than that of binary oxide nanosheets due to their more complex composition. For example, $TiNb_2O_7$ nanosheets have not been reported, despite being a very promising LIB anode material. Facile methods for the synthesis of ternary oxide nanosheets need to be developed to advance their energy storage applications.

Several approaches have been previously reported for the synthesis of ternary oxide nanosheets. Exfoliation was used to synthesize ternary oxide nanosheets from their layered bulk counterparts. Titanium niobium oxide nanosheets, such as $TiNbO_5^-$ and $Ti_2NbO_7^-$, were prepared by exfoliating protonated cation-exchangeable layered oxides, such as $KTiNbO_5$ and $CsTi_2NbO_7$, using tetra(n-butylammonium) hydroxide [24-26]. $[Mn_{1/3}Co_{1/3}Ni_{1/3}]O_2$ nanosheets were synthesized by proton exchange of $Li[Mn_{1/3}Co_{1/3}Ni_{1/3}]O_2$, followed by exfoliation using tetramethylammonium hydroxide [27]. Another strategy for ternary oxide nanosheet synthesis involves the solvothermal approach, whereby the precursors are dissolved in an appropriate solvent such as hydroethanolic solution or ethylene glycol, and then reacted in autoclave, forming an intermediate product that is calcined to form the desired oxide [8, 14, 28]. Ternary oxide nanosheets were also synthesized by electrodeposition on conductive substrates. $NiCo_2O_4$ nanosheets were electrodeposited on Ni foam at a potential of − 1.0 V vs. saturated calomel electrode, whereby Ni and Co reacted with OH^- that was formed during the electrochemical reaction. This led to the synthesis of nickel cobalt hydroxide, which was converted to the corresponding oxide by calcination [20]. Similar electrochemical deposition process was also reported for the synthesis of $MnCo_2O_4$ nanosheets [29].

Despite the promising energy storage performance of ternary oxide nanosheets, their current synthesis methods suffer from several limitations. Exfoliation is time-consuming; the process may take up to one month. It is also not environmentally friendly since it involves a protonation step using a concentrated acid solution [24, 25, 27]. In addition, this synthesis process is only limited to intrinsically layered oxides, such as $TiNbO_5^-$ and $Ti_2NbO_7^-$. The solvothermal and electrodeposition methods are difficult to scale up, and do not provide a general platform for ternary oxide nanosheet synthesis. Although several methods for the generalized synthesis of binary oxide nanosheets have been reported [30-35], they have not been extended to cover the more complex ternary oxides.

Herein the GO planar-confined growth strategy, which we have recently reported for the generalized synthesis of binary oxide nanosheets [36], is extended to the synthesis of ternary oxide nanosheets. Metal oxide precursors were mixed with GO at the desired ratios, followed by washing, drying and calcination, leading to the formation of ternary oxide

nanosheets. The metal oxide precursor ratio and calcination conditions were used to control the composition, phase, crystallite size, surface area, porosity and rGO content of the nanosheets. In addition, the nanosheets could be further anchored to rGO sheets upon synthesis using the opposite-charge method (OCM). The simplicity and versatility of the GO-templated synthesis of ternary oxide nanosheet overcome the challenges associated with the previously reported methods. The resulting ternary oxide nanosheets demonstrated very good performance as LIB anodes.

2. Materials and Methods

The ternary oxide and ternary oxide/rGO nanosheets were synthesized using GO planar-confined growth strategy and opposite-charge method, which were described in our previous work [36]. The detailed synthesis conditions are described below.

2.1. Synthesis of $TiNb_2O_7$ nanosheets

0.89 mmol of Ti(IV) butoxide and 2.07 mml of Nb(V) ethoxide were added to a 240-mL dispersion of GO in absolute ethanol (0.5 mg/mL), and stirred overnight at room temperature. The GO/precursor complex was separated by centrifugation, washed twice using ethanol at room temperature, and dried overnight at 60 °C. The dry GO/precursor complex was finally calcined at 700 °C for 1 h in air to produce the nanosheets.

2.2. Synthesis of $Ti_{0.61}Nb_{1.29}O_4$ nanosheets

$Ti_{0.61}Nb_{1.29}O_4$ nanosheets were synthesized in a similar manner as $TiNb_2O_7$ nanosheets, except that calcination was conducted at 700 °C for 2 h in Ar to produce $Ti_{0.61}Nb_{1.29}O_4$/rGO nanosheets. The retained rGO was removed by further calcination at 500 °C for 1 h in air.

2.3. Synthesis of $TiNb_2O_7$/rGO-OCM and $Ti_{0.61}Nb_{1.29}O_4$/rGO-OCM nanosheets

Positively charged GO-PDDA was synthesized according to our previous report [36]. Aqueous GO-PDDA dispersion (0.5 mg/mL) was mixed with negatively charged $TiNb_2O_7$ and $Ti_{0.61}Nb_{1.29}O_4$ nanosheets dispersed in deionized water at a concentration 0.4 mg/mL, resulting in spontaneous aggregation due to electrostatic interaction. The nanocomposite was separated by centrifugation, dried overnight at 60 °C, and calcined at 400 °C for 1 h in Ar.

2.4. Synthesis of $Ni_xCo_{3-x}O_4$ nanosheets

Ni(II) acetylacetonate and Co(II) acetylacetonate were added at molar ratios of 0.5, 1, 2 and 4 (total number of mmoles = 2.96) to a 240-mL dispersion of GO in absolute ethanol (0.5 mg/mL), and stirred overnight at 45 °C. The GO/precursor complex was separated by centrifugation at 40 °C, washed twice using warm ethanol (~45 °C), and dried overnight at 60 °C. The dry GO/precursor complex was finally calcined at 400 °C and 350 °C for 1 h in air to produce the nanosheets. $Ni_{1.29}Co_{1.71}O_4$/rGO nanosheets were calcined at 325 °C for 0.8 h in air instead.

2.5. Synthesis of $Mn_xCo_{3-x}O_4$ nanosheets

Mn(II) acetylacetonate and Co(II) acetylacetonate were added at molar ratios of 0.05, 0.1, 0.15 and 0.2 (total number of mmoles = 2.96) to a 240-mL dispersion of GO in absolute ethanol (0.5 mg/mL), and stirred overnight at 45 °C. The GO/precursor complex was separated by centrifugation at 40 °C, washed twice using warm ethanol (~45 °C), and dried overnight at 60 °C. The dry GO/precursor complex was finally calcined at 500 °C for 1 h in air to produce the nanosheets. $Mn_{1.08}Co_{1.92}O_4$/rGO nanosheets were calcined at 325 °C for 0.3 h in air instead.

2.6. Materials Characterization

The nanosheets were characterized using TEM (FEI Tecnai F20), XRD (Bruker D8 ADVANCE), TGA (PerkinElmer Pyris 1 TGA), EDX (OXFORD X-Max^N), N_2 adsorption-desorption (Micromeritics ASAP 2020), Zetasizer Nano-SZ (Malvern Instruments), AFM (Bruker Dimension ICON AFM, non-contact/tapping mode) and XPS (VG ESCALAB 220i-XL).

2.7. Electrochemical Measurements

The nanosheets were mixed with vapor-grown carbon fibers and polyvinylidene fluoride at a ratio of 7:2:1 (by weight). The solid mixture was dispersed in *N*-methyl-2-pyrrolidone forming a slurry, which was coated on coper foil, dried at 90 °C, and then pressed. The dry coated copper foil was cut into discs with 12.7 mm diameter, and assembled in an Ar-filled glove box, with Li metal used as the counter electrode. 1 M $LiPF_6$ in ethylene carbonate and diethyl carbonate (1:1 by volume) was used as electrolyte. CV was conducted at a scan rate of 0.1 mV/s and a voltage range of 1– 3 V vsersus Li^+/Li for $TiNb_2O_7$ and

$Ti_{0.61}Nb_{1.29}O_4$ nanosheets, and 0.005− 3 V versus Li^+/Li for $Ni_{1.29}Co_{1.71}O_4$ and $Mn_{1.08}Co_{1.92}O_4$ nanosheets. Galvanostatic charge/discharge measurements were carried out at the above-mentioned voltage ranges with various current densities. Electrochemical impedance spectroscopy was conducted in the frequency range of 100 kHz to 10 mHz, with a voltage amplitude of 10 mV.

3. Results and Discussion

3.1. Materials Characterization

3.1.1. Titanium Niobium Oxide Nanosheets

$TiNb_2O_7$ nanosheets were synthesized using the GO planar-confined growth approach. We have previously demonstrated that Nb_2O_5 nanosheets could be doped with Ti up to 25 at% Ti [36]. It was observed that when Ti at% increased to ~33 at%, the phase changed from orthorhombic Nb_2O_5 to monoclinic $TiNb_2O_7$ (JCPDS #01-077-1374), with no remnant Nb_2O_5 phase or additional TiO_2 phase formation, as determined by X-ray diffractometry (XRD) (Figure 1g). The nanosheet morphology was investigated using transmission electron microscopy (TEM) (Figure 1a). The $TiNb_2O_7$ phase was confirmed by high-resolution TEM (HRTEM) (Figure 1b), which showed its (110) plane, as well as by selected area electron diffraction (SAED) pattern (Figure 1c). Energy dispersive X-ray (EDX) spectroscopy mapping showed the uniform distributions of Ti (Figure 1e) and Nb (Figure 1f), confirming the absence of phase separation. X-ray photoelectron spectroscopy (XPS) Ti core level spectrum (Figure 1i) showed a peak doublet at 464.6 eV and 458.9 eV (separated by 5.7 eV), corresponding to Ti $2p_{1/2}$ and Ti $2p_{3/2}$ of Ti^{4+} state, respectively [37, 38]. Nb core level spectrum (Figure 1j) showed a peak doublet at 210.0 eV and 207.3 eV (separated by 2.7 eV), corresponding to Nb $3d_{3/2}$ and Nb $3d_{5/2}$ of Nb^{5+}, respectively [39]. The chemical states of Ti and Nb agreed with previously reported results of $TiNb_2O_7$ [40]. The nanosheets were free from residual rGO content as shown by the thermogravimetric analysis (TGA) profile (Figure 1h). The nanosheets have a small crystallite size of 14.9 nm, moderate surface area and pore volume of 23.8 m^2/g (Figure S1a) and 0.1 cm^3/g (Figure S1b), respectively. Atomic force microscopy (AFM) analysis (Figure S1c) showed that the nanosheets have a nanothickness of ~3.5 nm.

The ability of the GO planar-confined growth strategy to produce ternary oxide nanosheets showed that GO not only served as a template, but also as a substrate on which metal oxide precursors could react to form complex phases, while growing into a 2D nanostructure. To the best of our knowledge, this is the first report of the synthesis of $TiNb_2O_7$ nanosheets. It shows the significance of the synthesis methodology; its broad applicability and versatility allow the facile synthesis of complex oxides as nanosheets for potential applications in various fields.

Upon using the same precursor ratio and synthesis conditions for $TiNb_2O_7$ nanosheets, but changing calcination conditions from 700 °C/1 h/ air to 700 °C/2 h/Ar, a different phase was obtained. Under the oxygen-deficient conditions, $Ti_{0.61}Nb_{1.29}O_4$/rGO nanosheets with tetragonal $Ti_{0.95}Nb_{0.95}O_4$ phase were synthesized. This could be attributed to the inert atmosphere that prevented further oxidation to $TiNb_2O_7$. TEM showed the nanosheet morphology of the nanocomposite (Figure 2a, b), which is composed of $Ti_{0.61}Nb_{1.29}O_4$ nanoparticles anchored to rGO sheets. The $Ti_{0.95}Nb_{0.95}O_4$ phase (JCPDS #00-047-0024) was determined by XRD (Figure 2d), and confirmed by HRTEM (Figure 2c) that showed its (110) plane. The full rGO content was retained in the nanocomposite because of the inert calcination conditions, and it was calculated to be 36.1 wt% using TGA (Figure 2e). XPS Ti (Figure 2f) and Nb (Figure 2g) core level spectra shifted to higher binding energies. This has been previously reported for rGO-incorporated nanocomposites, and has been attributed to the interaction between the residual oxygenated groups on rGO and the metal species, which resulted in electron density withdrawal from the metal species, leading to a peak shift to higher binding energies [38, 41]. Ti core level spectrum showed the main peak doublet at 465.6 eV and 459.8 eV, corresponding to Ti $2p_{1/2}$ and Ti $2p_{3/2}$, respectively. Ti $2p_{3/2}$ peak was deconvoluted into two peaks at 459.9 eV and 458.9 eV, which could be assigned to Ti^{4+} and Ti^{3+}, respectively [42]. Nb core level spectrum doublet appeared at 210.8 eV and 208.1 eV, corresponding to Nb $3d_{3/2}$ and Nb $3d_{5/2}$, respectively. Nb $3d_{5/2}$ was deconvoluted into two peaks at 208.1 eV and 207.1 eV, which could be attributed to Nb^{5+} and Nb^{4+}, respectively [39]. The presence of the lower Ti and Nb oxidation states agreed with the oxygen-deficient phase.

Pure $Ti_{0.61}Nb_{1.29}O_4$ nanosheets could be synthesized by removing rGO. This could be done by calcining the nanocomposite at 500 °C/1 h/air, which was enough to remove the rGO, leaving behind pure $Ti_{0.61}Nb_{1.29}O_4$ nanosheets (Figure 3a), free from residual rGO (Figure 3h). Interestingly, the $Ti_{0.95}Nb_{0.95}O_4$ phase was still stable after calcination in air at 500 °C, as shown by XRD pattern (Figure 3g), HRTEM (Figure 3b) and SAED pattern

(Figure 3c). EDX analysis showed the uniform distribution of Ti (Figure 3e) and Nb (Figure 3f) throughout the nanosheets. $Ti_{0.61}Nb_{1.29}O_4$ nanosheets have a relatively small crystallite size of 8.0 nm, and were mesoporous with an average pore size of 5 nm (Figure 3j). They also displayed a large pore volume of 0.23 cm^3/g and a high specific surface area of 98.7 m^2/g (Figure 3i). As far as we know, $Ti_{0.95}Nb_{0.95}O_4$ tetragonal phase was not previously synthesized as nanosheets.

$TiNb_2O_7$/rGO and $Ti_{0.61}Nb_{1.29}O_4$/rGO nanosheets were synthesized using OCM, where the metal oxide nanosheets interacted with functionalized GO electrostatically. $TiNb_2O_7$ and $Ti_{0.61}Nb_{1.29}O_4$ nanosheets have negative surface charges of ~– 40 mV and ~– 45mV, respectively (Figure S2). They reacted electrostatically with the positively charged GO– PDDA complex, followed by calcination in Ar, resulting in the formation of $TiNb_2O_7$/rGO and $Ti_{0.61}Nb_{1.29}O_4$/rGO nanosheets. The intimate contact between the metal oxide and rGO sheets is clearly observed in the TEM (Figure S3a, b) and EDX mapping images (Figure S3d– f, h– j). The monoclinic and tetragonal phases of $TiNb_2O_7$ and $Ti_{0.61}Nb_{1.29}O_4$, respectively, were not changed after rGO incorporation (Figure S3k, l). The rGO content, calculated using TGA (Figure S3m), was 23.8 and 27.0 wt% for $TiNb_2O_7$/rGO-OCM and $Ti_{0.61}Nb_{1.29}O_4$/rGO-OCM, respectively.

3.1.2. $Ni_xCo_{3-x}O_4$ and $Mn_xCo_{3-x}O_4$ nanosheets

$Ni_xCo_{3-x}O_4$ nanosheets of different compositions were synthesized using the GO planar-confined growth strategy at 400 °C/1 h/ air. The nanosheet morphology was observed at all compositions (Figure 4a– d), and the uniform elemental distribution was confirmed by EDX mapping (Figure 4e– l). It was found that the $Ni_xCo_{3-x}O_4$ nanosheets synthesized using Ni:Co precursor molar ratios of 0.5, 1, 2 and 4 have actual Ni:Co molar ratios of 0.08, 0.22, 0.38 and 0.75, respectively, as calculated using EDX analysis. The discrepancy could be explained by the different affinity of both precursors to the GO surface, which led to different amounts of the precursors being retained after washing. These results showed that cobalt acetyl acetonate has ~5 times higher affinity than nickel acetyl acetonate towards the GO surface. XRD showed that $Ni_{0.22}Co_{2.78}O_4$ (Ni/Co = 0.08) crystallized into Co_3O_4 phase (JCPDS # 00-042-1467) (Figure 4m), while the compositions with higher Ni content crystallized into $NiCo_2O_4$ (JCPDS # 00-020-0781) phase (Figure 4n). In $Ni_{0.22}Co_{2.78}O_4$, Ni ions only replaced a portion of the cobalt ions in the Co_3O_4 phase. As the Ni/Co ratio increased, there was a phase change to $NiCo_2O_4$ (JCPDS # 00-020-0781) to accommodate more Ni ions. The ability to control the composition of the ternary oxide nanosheets

demonstrated the versatility of the synthesis method, which allowed fine tuning of the composition for the intended application.

$Ni_{1.29}Co_{1.71}O_4$ nanosheets were further synthesized using lower calcination temperatures (350 °C/1 h/air and 325 °C/0.8 h/air) to obtain smaller crystallite size and higher rGO content. The nanosheet morphology was confirmed using TEM at both synthesis conditions (Figure S4a, c). The nanosheets synthesized at 350 °C/1 h/air crystallized into the $NiCo_2O_4$ phase as shown by XRD (Figure S4e) and SAED (Figure S4b). They have a small crystallite size of 4.5 nm, but were almost devoid of rGO (Figure S4f). The nanosheets synthesized at 325 °C/0.8 h/air have a much higher rGO content of 31.3 wt% (Figure S4f). They showed relatively low crystallinity as demonstrated by the weak XRD peaks (Figure S4e) and faint SAED pattern (Figure S4d), however, their crystalline phase could still be determined to be $NiCo_2O_4$, with a crystallite size of 4.2 nm.

$Mn_xCo_{3-x}O_4$ nanosheets were synthesized at 500 °C/1 h/air using Mn/Co molar ratios of 0.05, 0.1, 0.15 and 0.2, and were obtained with actual Mn/Co molar ratios of 0.56 and 1.12, 1.67 and 2.33, respectively. These results indicated the very high affinity of manganese acetyl acetonate to GO, where the actual Mn/Co molar ratio was always ~11 times that of the precursor molar ratio. TEM showed that the nanosheet morphology was obtained at all compositions (Figure 5a– d), and EDX mapping images demonstrated the uniform distribution of the elements (Figure 5e– l). The nanosheets crystallized into cubic Co_2MnO_4 (JCPDS #00-001-1130) and $MnCo_2O_4$ (JCPDS #00-023-1237) phases for $Mn_{1.08}Co_{1.92}O_4$ and $Mn_{1.58}Co_{1.42}O_4$, respectively (Figure 5m), and into tetragonal $(Co,Mn)(Co,Mn)_2O_4$ phase (JCPDS # 00-018-0408) for $Mn_{1.88}Co_{1.12}O_4$ and $Mn_{2.10}Co_{0.90}O_4$ (Figure 5n). $Mn_{1.08}Co_{1.92}O_4$ nanosheets were further analyzed via SAED (Figure S5a), confirming their cubic Co_2MnO_4 phase.

At lower synthesis conditions of 325 °C/0.3 h/air, $Mn_{1.08}Co_{1.92}O_4$/rGO nanosheets were synthesized (Figure S5b). XRD (Figure S5c) and SAED (Figure S5b: inset) showed their cubic spinel phase. The crystallite size was calculated to be 5.3 nm, as compared to 6.8 nm for the nanosheets synthesized at 500 °C/1 h/air. The rGO content was calculated using TGA (Figure S5d), with 38.4 wt% rGO retained in the nanocomposite, as compared to ~2.9 wt% for the nanosheets synthesized at 500 °C/1 h/air. The synthesis conditions and properties of $TiNb_2O_7$, $Ti_{0.61}Nb_{1.29}O_4$, $Ni_{1.29}Co_{1.71}O_4$ and $Mn_{1.08}Co_{1.92}O_4$ nanosheets are summarized in Table 1.

3.2. Li-ion Battery Anode Performance

3.2.1. Titanium Niobium Oxide Nanosheets

$TiNb_2O_7$ nanosheets showed a relatively stable LIB anode cycling performance at 1C (Figure 6a), achieving a capacity of ~144 mAh/g after 100 cycles, which slightly improved upon rGO incorporation, reaching ~151 mAh/g. The high Coulombic efficiency of 99− 100% exhibited by $TiNb_2O_7$/rGO-OCM nanosheets after the first few cycles indicated very good stability profile. The rate study (Figure 6b) showed that $TiNb_2O_7$ and $TiNb_2O_7$/rGO-OCM nanosheets have similar performance at the relatively low rates of 0.5C and 1C, however, $TiNb_2O_7$/rGO-OCM nanosheets demonstrated better performance at higher rates, achieving ~137, ~103 and ~84 mAh/g, as compared to ~120, ~83 and ~63 mAh/g shown by $TiNb_2O_7$ nanosheets, at 5C, 10C and 15C, respectively. This could be ascribed to the higher conductivity of $TiNb_2O_7$/rGO-OCM nanosheets, as demonstrated by the smaller semi-circle diameter in the Nyquist plots (Figure S6a).

Cyclic voltammetry (CV) was conducted at 1− 3 V to study the redox processes of $TiNb_2O_7$/rGO-OCM nanosheets (Figure S6b). The main cathodic and anodic peaks appeared at 1.49 V and 1.74 V, respectively, which were assigned to Nb^{5+}/Nb^{4+} redox couple. A weak pair of redox peaks could be seen at 1.83 V and 1.97 V, corresponding to Ti^{4+}/Ti^{3+} redox couple. The redox reactions involving Nb^{4+}/Nb^{3+} redox couple could take place at 1− 1.4 V. The prominence of the Nb^{5+}/Nb^{4+} redox peaks, and the weakness of those of Ti^{4+}/Ti^{3+} and Nb^{4+}/Nb^{3+} redox couples agreed with previously reported results [12]. The sloping galvanostatic charge-discharge (GCD) curves (Figure S6c) agreed with the broad CV peaks, and with previous reports [11, 12]. Charge storage mechanism was determined by the analysis of CV data at increasing scan rates, according to the following equation,

$$I = av^b \qquad \text{Eq. 1}$$

where I is the current intensity in A, v is the potential scan rate in V/s, while a and b are adjustable parameters. The value of b indicates the charge storage mechanism; b = 1 in the case of capacitive storage, and b = 0.5 in the case of diffusion-limited storage [43]. The b value of 0.76 shown in Figure S6d indicated that the charge storage mechanism is both diffusion-controlled and capacitive. The capacitive contribution could explain the very good rate capability achieved by the nanosheets.

$TiNb_2O_7$/rGO-OCM nanosheets showed better performance than $TiNb_2O_7$ nanofibers [44] and $TiNb_2O_7$ nanoparticles [11] (which achieved ~150 and ~76 mAh/g at 2.6C and 10C,

respectively), and have comparable performance to $TiNb_2O_7$/graphene nanocomposite [12] and $TiNb_2O_7$@C microwires [45] (which have capacities of 136 and ~75 mAh/g at 8C and 15C, respectively) (Table S1).

Upon introduction of $TiNb_2O_7$ as Li-ion battery anode, several other titanium niobium oxides such as $Ti_2Nb_{10}O_{29}$ [46-48], $TiNb_6O_{17}$ [49] and $Ti_2Nb_2O_9$ [50] were reported. Although some of these oxides have very promising performance, for example $Ti_2Nb_{10}O_{29}$ (theoretical capacity = 396 mAh/g) achieved 132 and 50 mAh/g at 20C (7.9 A/g) and 50C (19.8 A/g), respectively [46], studies on these materials remain limited. $Ti_{0.61}Nb_{1.29}O_4$ with the tetragonal $Ti_{0.95}Nb_{1.95}O_4$ crystal structure has not been previously studied as LIB anode. However, it is a promising material due to its high theoretical capacity of ~402 mAh/g, assuming the involvement of Nb^{5+}/Nb^{4+}, Nb^{4+}/Nb^{3+} and Ti^{4+}/Ti^{3+} redox couples.

$Ti_{0.61}Nb_{1.29}O_4$ nanosheets showed a very promising LIB anode performance. They have a stable cycling performance at 0.5C (Figure 6c), reaching ~149 mAh/g after 100 cycles. The low Coulombic efficiency at the first cycle, implying irreversible capacity during the first discharge, could be attributed to the high surface area of the $Ti_{0.61}Nb_{1.29}O_4$ nanosheets (98.7 m^2/g) [12]. rGO incorporation did not improve the electrode performance at low rates. However, $Ti_{0.61}Nb_{1.29}O_4$/rGO-OCM nanosheets have better performance at high rates (Figure 6d), achieving ~66 and ~40 mAh/g, as compared to ~47 and ~20 mAh/g obtained by pure $Ti_{0.61}Nb_{1.29}O_4$ nanosheets, at 15C and 25C, respectively. $Ti_{0.61}Nb_{1.29}O_4$/rGO-OCM nanosheets have a comparable rate performance as $TiNb_2O_7$/rGO-OCM nanosheets, indicating that $Ti_{0.61}Nb_{1.29}O_4$ is a very promising LIB anode material.

CV of $Ti_{0.61}Nb_{1.29}O_4$/rGO-OCM nanosheets showed two main peaks at 1.55 V and 1.82 V (Figure S7a), which could be attributed to Nb^{5+}/Nb^{4+} redox couple, as previously shown for $TiNb_2O_7$. However, no other distinct peaks were observed, which could be due to their broad and weak nature. GCD profile (Figure S7b) showed sloping curves, which was similar to $TiNb_2O_7$. Interestingly, the charge storage mechanism also involved capacitive contribution as indicated by the *b* value of 0.77 (Figure S7c).

3.2.2. $Ni_{1.29}Co_{1.71}O_4$ and $Mn_{1.08}Co_{1.92}O_4$ nanosheets

$Ni_{1.29}Co_{1.71}O_4$ nanosheets synthesized at 350 °C/1 h/air were studied using CV. They have the main cathodic CV peak at ~0.72 V during the initial discharge, which was ascribed to the decomposition of $Ni_{1.29}Co_{1.71}O_4$ forming metallic Ni and Co within Li_2O matrix, and also to SEI formation (Figure S8a) [51]. This peak showed a marked decrease in intensity and shifted to ~1 V during the second and third cycles. The lower intensity is due to the

irreversible SEI formation during the first cycle, while the peak shift could be due to an initial activation process [23]. The anodic peaks at ~1.5 V and ~2.2 V were attributed to partial SEI decomposition [52] and metallic Ni and Co oxidation [8], respectively. The GCD profile (Figure S8c) agreed with the CV curves. The reactions taking place during lithiation and de-lithiation could be expressed as follows [8, 51],

$$Ni_{1.29}Co_{1.71}O_4 + 8Li^+ + 8e^- \rightarrow 1.29Ni + 1.71Co + 4Li_2O \quad \text{Eq. 2}$$

$$Ni + Li_2O \leftrightharpoons NiO + 2Li^+ + 2e^- \quad \text{Eq. 3}$$

$$Co + Li_2O \leftrightharpoons CoO + 2Li^+ + 2e^- \quad \text{Eq. 4}$$

$$3CoO + Li_2O \leftrightharpoons Co_3O_4 + 2Li^+ + 2e^- \quad \text{Eq. 5}$$

$Ni_{1.29}Co_{1.71}O_4$ nanosheets showed rapid capacity decline, reaching ~306 and ~110 mAh/g after 50 and 100 cycles at 0.1 and 1 A/g, respectively (Figure 7a, b). The introduction of rGO to $Ni_{1.29}Co_{1.71}O_4$ nanosheets by adjusting the calcination conditions to 325 °C/0.8 h/air dramatically improved the cycling performance. A high capacity of 1531 mAh/g was achieved by $Ni_{1.29}Co_{1.71}O_4$/rGO after 50 cycles at 0.1 A/g (Figure 7a). At the higher current density of 1 A/g, the specific capacity showed an initial decline during the first 20 cycles, and then it stabilized with a slight increase during further cycling, reaching ~506 mAh/g after 100 cycles, with a Coulombic efficiency of 98– 99% (Figure 7b). Capacity increase over cycling of conversion-based materials has been previously observed, with several explanations reported, including electrolyte decomposition at low potentials forming a gel-like polymer that dissolved upon charging [53-55], irreversible Li_2O formation during the initial cycles, followed by gradual activation over cycling [56], and continuous pulverization and particle size reduction during cycling, exposing more electrochemically active sites [57, 58]. Rate capability of $Ni_{1.29}Co_{1.71}O_4$ nanosheets was studied at a current density range of 0.5– 5 A/g. They retained ~128 and ~48 mAh/g, which improved to ~291 and ~147 mAh/g upon rGO incorporation, at 2 and 4 A/g, respectively (Figure S8e).

$Ni_{1.29}Co_{1.71}O_4$/rGO nanosheets have a high capacity of ~913 mAh/g at 0.5 A/g, which was better than or comparable to that achieved by other $NiCo_2O_4$ nanocomposites [13, 23, 51]. $Ni_{1.29}Co_{1.71}O_4$/rGO nanosheets have a good capacity of ~291 mAh/g at 2 A/g, which was comparable to $NiCo_2O_4$ nanoplates/rGO [13], $NiCo_2O_4$ nanosheets/multiwall carbon nanotubes [51] and $NiCo_2O_4$ nanosheets/rGO [23], which showed 396, 392 and ~437 mAh/g at 0.8 A/g, 1 A/g and 1 A/g, respectively (Table S1).

$Mn_{1.08}Co_{1.92}O_4$ nanosheets synthesized at 500 °C/1 h/air showed a broad CV peak at ~1.4 V and a sharp peak at ~0.55 V (Figure S8b). The former was attributed to Li^+ insertion into the lattice and reduction of Co^{3+} to Co^{2+}, while the latter was ascribed to the decomposition of the material forming Li_2O with embedded metallic Mn and Co [6, 59]. The cathodic reduction potential shifted to ~0.88 V during the second cycle as a result of material activation [6, 60]. The anodic peaks at ~1.5 and ~2 V could be due to Mn and Co oxidation, respectively [6, 9, 61]. These redox processes were also reflected by the GCD profile (Figure S8d), which matched the CV curves. The entire electrochemical process could be expressed as follows [6, 9, 60],

$$Mn_{1.08}Co_{1.92}O_4 + 8Li^+ + 8e^- \rightarrow 1.08Mn + 1.92Co + 4Li_2O \quad \text{Eq. 6}$$

$$1.08Mn + 1.92Co + 3Li_2O \leftrightharpoons 1.08MnO + 1.92CoO + 6Li^+ + 6e^- \quad \text{Eq. 7}$$

$Mn_{1.08}Co_{1.92}O_4$ nanosheets showed rapid capacity decay, achieving ~229 and ~151 mAh/g after 50 and 100 cycles at 0.1 and 1 A/g, respectively (Figure 7c, d). This drastic capacity decay was mitigated by the incorporation of rGO within $Mn_{1.08}Co_{1.92}O_4$ nanosheets. $Mn_{1.08}Co_{1.92}O_4$/rGO nanosheets showed excellent stability at 0.1 A/g, achieving ~1118 mAh/g after 50 cycles (Figure 7c). At 1 A/g, they suffered from some capacity decline over the first 25 cycles, then the capacity increased to ~435 mAh/g after 100 cycles (Figure 7d). $Mn_{1.08}Co_{1.92}O_4$ nanosheets also improved in rate capability by rGO incorporation, achieving ~1020, ~372, ~196 and ~160 mAh/g at 0.5, 2, 4 and 5 A/g, respectively (Figure S8f), which was better than or comparable to previously reported results (Table S1).

Overall, the ternary oxide nanosheets have achieved very promising LIB anode performance. Ternary oxide nanosheets operating by intercalation/de-intercalation mechanism ($TiNb_2O_7$ and $Ti_{0.61}Nb_{1.29}O_4$) showed stable cycling and very good rate capability, which were attributed to the small thickness and 2D structure that facilitated charge transport and mitigated volume change. In addition, the incorporation of rGO allowed for a better performance at high rates. The conversion reaction-based ternary oxide nanosheets ($Ni_{1.29}Co_{1.71}O_4$ and $Mn_{1.08}Co_{1.92}O_4$) showed rapid capacity decay, which was mitigated by rGO incorporation, mainly due to the ability of rGO sheets to prevent pulverization-induced contact loss and improve conductivity.

Our facile, versatile synthesis methodology would facilitate ternary oxide nanosheet applications in energy storage. Our materials could be further developed for more practical

applications; for example, the nanosheets' tap density could be optimized by adjusting the nanosheets' attributes or assembling them into 3D microstructures.

4. Conclusion

We have demonstrated that the GO planar-confined growth strategy could be broadly applied to the synthesis of ternary oxide nanosheets, which were rarely reported previously. The synthesis conditions were used to control the nanosheet characteristics, such as composition, phase and rGO content. The variety of ternary oxide nanosheets obtained was applied as LIB anodes. Insertion-based ternary oxide nanosheets, including $TiNb_2O_7$ and $Ti_{0.61}Nb_{1.29}O_4$, achieved high capacity and stable performance, which were further improved by rGO incorporation, especially at high current densities. Conversion reaction-based ternary oxide nanosheets, including $Ni_{1.29}Co_{1.71}O_4$ and $Mn_{1.08}Co_{1.92}O_4$, showed pulverization-induced capacity decay, which was mitigated by rGO incorporation, achieving high capacities over prolonged cycling and better rate capability.

Appendix: Supplementary Data

Supplementary data associated with this article can be found in the online version at http://www.journals.elsevier.com/nano-energy.

Acknowledgements

The authors thank Dr. Jinhua Yang and Dr. Xun Yuan of the Institute of Bioengineering and Nanotechnology (IBN) for helpful discussions. This work was funded by IBN (Biomedical Research Council, Agency for Science, Technology and Research, Singapore).

References

[1] D. Kong, W. Ren, Y. Luo, Y. Yang, C. Cheng, J. Mater. Chem. A, 2 (2014) 20221-20230.

[2] J.-T. Han, Y.-H. Huang, J.B. Goodenough, Chem. Mater., 23 (2011) 2027-2029.

[3] K. Tang, X. Mu, P.A. van Aken, Y. Yu, J. Maier, Adv. Energy Mater., 3 (2013) 49-53.

[4] J. Liu, C. Liu, Y. Wan, W. Liu, Z. Ma, S. Ji, J. Wang, Y. Zhou, P. Hodgson, Y. Li, CrystEngComm, 15 (2013) 1578-1585.

[5] G. Huang, S. Xu, Z. Xu, H. Sun, L. Li, ACS Appl. Mater. Interfaces, 6 (2014) 21325-21334.

[6] J. Li, S. Xiong, X. Li, Y. Qian, Nanoscale, 5 (2013) 2045-2054.

[7] L. Shen, Q. Che, H. Li, X. Zhang, Adv. Funct. Mater., 24 (2014) 2630-2637.

[8] F. Zheng, D. Zhu, Q. Chen, ACS Appl. Mater. Interfaces, 6 (2014) 9256-9264.

[9] C. Fu, G. Li, D. Luo, X. Huang, J. Zheng, L. Li, ACS Appl. Mater. Interfaces, 6 (2014) 2439-2449.

[10] L. Yu, L. Zhang, H.B. Wu, G. Zhang, X.W. Lou, Energy Environ. Sci., 6 (2013) 2664-2671.

[11] L. Fei, Y. Xu, X. Wu, Y. Li, P. Xie, S. Deng, S. Smirnov, H. Luo, Nanoscale, 5 (2013) 11102-11107.

[12] S. Li, X. Cao, C.N. Schmidt, Q. Xu, E. Uchaker, Y. Pei, G. Cao, J. Mater. Chem. A, 4 (2016) 4242-4251.

[13] Y. Chen, M. Zhuo, J. Deng, Z. Xu, Q. Li, T. Wang, J. Mater. Chem. A, 2 (2014) 4449-4456.

[14] X. Hou, X. Wang, B. Liu, Q. Wang, T. Luo, D. Chen, G. Shen, Nanoscale, 6 (2014) 8858-8864.

[15] L. Yao, J. Wu, H. Deng, Q.-A. Huang, Q. Su, G. Du, Mater. Lett., 180 (2016) 188-191.

[16] Y.-L. Ding, Y. Wen, P.A. van Aken, J. Maier, Y. Yu, Small, 11 (2015) 2011-2018.

[17] X. Liu, W. Si, J. Zhang, X. Sun, J. Deng, S. Baunack, S. Oswald, L. Liu, C. Yan, O.G. Schmidt, Sci. Rep., 4 (2014) 7452.

[18] D. Rangappa, K.D. Murukanahally, T. Tomai, A. Unemoto, I. Honma, Nano Lett., 12 (2012) 1146-1151.

[19] Y. Zhu, C. Cao, S. Tao, W. Chu, Z. Wu, Y. Li, Sci. Rep., 4 (2014) 5787.

[20] C. Yuan, J. Li, L. Hou, X. Zhang, L. Shen, X.W. Lou, Adv. Funct. Mater., 22 (2012) 4592-4597.

[21] X. Rui, X. Zhao, Z. Lu, H. Tan, D. Sim, H.H. Hng, R. Yazami, T.M. Lim, Q. Yan, ACS Nano, 7 (2013) 5637-5646.

[22] J. Mu, B. Chen, Z. Guo, M. Zhang, Z. Zhang, P. Zhang, C. Shao, Y. Liu, Nanoscale, 3 (2011) 5034-5040.

[23] G. Gao, H.B. Wu, X.W.D. Lou, Adv. Energy Mater., 4 (2014) 1400422.

[24] A. Takagaki, T. Yoshida, D. Lu, J.N. Kondo, M. Hara, K. Domen, S. Hayashi, J. Phys. Chem. B, 108 (2004) 11549-11555.

[25] A.S. Dias, S. Lima, D. Carriazo, V. Rives, M. Pillinger, A.A. Valente, J. Catal., 244 (2006) 230-237.

[26] M. Osada, G. Takanashi, B.-W. Li, K. Akatsuka, Y. Ebina, K. Ono, H. Funakubo, K. Takada, T. Sasaki, Adv. Funct. Mater., 21 (2011) 3482-3487.

[27] E.-J. Oh, T.W. Kim, K.M. Lee, M.-S. Song, A.-Y. Jee, S.T. Lim, H.-W. Ha, M. Lee, J.-H. Choy, S.-J. Hwang, ACS Nano, 4 (2010) 4437-4444.

[28] G. Huang, X. Guo, X. Cao, Q. Tian, H. Sun, J. Alloys Compd., 695 (2017) 2937–2944.

[29] K.K. Naik, R.T. Khare, M.A. More, D.J. Late, C.S. Rout, RSC Adv., 6 (2016) 29734-29740.

[30] S. Yang, X. Feng, K. Mullen, Adv. Mater., 23 (2011) 3575-3579.

[31] S. Yang, X. Feng, L. Wang, K. Tang, J. Maier, K. Mullen, Angew. Chem. Int. Ed., 49 (2010) 4795-4799.

[32] L. Wang, X. Bi, S. Yang, Adv. Mater., 28 (2016) 7672-7679.

[33] Z. Sun, T. Liao, Y. Dou, S.M. Hwang, M.S. Park, L. Jiang, J.H. Kim, S.X. Dou, Nat. Commun., 5 (2014) 3813.

[34] J. Zhu, Z. Yin, H. Li, H. Tan, C.L. Chow, H. Zhang, H.H. Hng, J. Ma, Q. Yan, Small, 7 (2011) 3458-3464.

[35] S. Takenaka, S. Miyake, S. Uwai, H. Matsune, M. Kishida, J. Phys. Chem. C, 119 (2015) 12445-12454.

[36] A.A. AbdelHamid, Y. Yu, J. Yang, J.Y. Ying, Adv. Mater., (2017) 1701427.

[37] Y. Li, Z. Wang, X.-J. Lv, J. Mater. Chem. A, 2 (2014) 15473-15479.

[38] M.S.A. Sher Shah, A.R. Park, K. Zhang, J.H. Park, P.J. Yoo, ACS Appl. Mater. Interfaces, 4 (2012) 3893-3901.

[39] A. Mozalev, R.M. Vázquez, C. Bittencourt, D. Cossement, F. Gispert-Guirado, E. Llobet, H. Habazaki, J. Mater. Chem. C, 2 (2014) 4847-4860.

[40] X. Lu, Z. Jian, Z. Fang, L. Gu, Y.-S. Hu, W. Chen, Z. Wang, L. Chen, Energy Environ. Sci., 4 (2011) 2638-2644.

[41] V. Etacheri, J.E. Yourey, B.M. Bartlett, ACS Nano, 8 (2014) 1491-1499.

[42] H. Zhang, Z. Xing, Y. Zhang, Z. Li, X. Wu, C. Liu, Q. Zhu, W. Zhou, RSC Adv., 5 (2015) 107150-107157.

[43] E. Lim, C. Jo, H. Kim, M.-H. Kim, Y. Mun, J. Chun, Y. Ye, J. Hwang, K.-S. Ha, K.C. Roh, K. Kang, S. Yoon, J. Lee, ACS Nano, 9 (2015) 7497-7505.

[44] V. Aravindan, J. Sundaramurthy, A. Jain, P.S. Kumar, W.C. Ling, S. Ramakrishna, M.P. Srinivasan, S. Madhavi, ChemSusChem, 7 (2014) 1858-1863.

[45] X. Wang, G. Shen, Nano Energy, 15 (2015) 104-115.

[46] Q. Cheng, J. Liang, Y. Zhu, L. Si, C. Guo, Y. Qian, J. Mater. Chem. A, 2 (2014) 17258-17262.

[47] X. Wu, J. Miao, W. Han, Y.-S. Hu, D. Chen, J.-S. Lee, J. Kim, L. Chen, Electrochem. Commun., 25 (2012) 39-42.

[48] T. Takashima, T. Tojo, R. Inada, Y. Sakurai, J. Power Sources, 276 (2015) 113-119.

[49] C. Lin, G. Wang, S. Lin, J. Li, L. Lu, Chem. Commun., 51 (2015) 8970-8973.

[50] J.F. Colin, V. Pralong, M. Hervieu, V. Caignaert, B. Raveau, Chem. Mater., 20 (2008) 1534-1540.

[51] A.K. Mondal, H. Liu, Z.-F. Li, G. Wang, Electrochim. Acta, 190 (2016) 346-353.

[52] H.S. Jadhav, G.M. Thorat, J. Mun, J.G. Seo, J. Power Sources, 302 (2016) 13-21.

[53] A. Ponrouch, P.-L. Taberna, P. Simon, M.R. Palacín, Electrochim. Acta, 61 (2012) 13-18.

[54] S. Laruelle, S. Grugeon, P. Poizot, M. Dollé, L. Dupont, J.M. Tarascon, J. Electrochem. Soc., 149 (2002) A627-A634.

[55] S. Grugeon, S. Laruelle, L. Dupont, J.M. Tarascon, Solid State Sci., 5 (2003) 895-904.

[56] J.-S. Do, C.-H. Weng, J. Power Sources, 146 (2005) 482-486.

[57] J. Luo, J. Liu, Z. Zeng, C.F. Ng, L. Ma, H. Zhang, J. Lin, Z. Shen, H.J. Fan, Nano Lett., 13 (2013) 6136-6143.

[58] A.A. AbdelHamid, X. Yang, J. Yang, X. Chen, J.Y. Ying, Nano Energy, 26 (2016) 425-437.

[59] C. Chen, B. Liu, Q. Ru, S. Ma, B. An, X. Hou, S. Hu, J. Power Sources, 326 (2016) 252-263.

[60] A.K. Mondal, D. Su, S. Chen, A. Ung, H.S. Kim, G. Wang, Chem. Eur. J., 21 (2015) 1526-1532.

[61] J. Ye, D. Zhao, Q. Hao, C. Xu, Electrochim. Acta, 222 (2016) 1402-1409.

Ayman A. AbdelHamid is a Postdoctoral Fellow at the Institute of Bioengineering and Nanotechnology (IBN), Singapore. He received his M.Sc. in Nanoscience and Technology from Nile University, Egypt in 2012, and his Ph.D. in Materials Science and Engineering from Nanyang Technological University, Singapore in 2017. His research interests include development of nanomaterials and nanocomposites for energy storage applications.

Jun Hui Soh is a Research Scientist at the Institute of Bioengineering and Nanotechnology (IBN), Singapore. He received his Ph.D. in Materials Research at the Imperial College of London. His research interests include development of novel nanomaterials for biomedical and energy applications.

Yue Yu received her Ph.D. in Chemical and Biomolecular Engineering from National University of Singapore in 2012, where she also spent three years as a Postdoctoral Research Fellow. She is currently a Postdoctoral Fellow at the Institute of Biomolecular and Nanotechnology. Her research interests include the development of nanomaterials for energy-related applications and studies on the structure-property relationship.

Jackie Y. Ying received her B.E. and Ph.D. from The Cooper Union and Princeton University, respectively. She joined the faculty at Massachusetts Institute of Technology in 1992, where she was Professor of Chemical Engineering until 2005. She has been the Founding Executive Director of the Institute of Bioengineering and Nanotechnology in Singapore since 2003. For her research on nanostructured materials, Prof. Ying has been recognized with the American Ceramic Society Ross C. Purdy Award, David and Lucile Packard Fellowship, Office of Naval Research Young Investigator Award, National Science Foundation Young Investigator Award, Camille Dreyfus Teacher-Scholar Award, American Chemical Society Faculty Fellowship Award in Solid-State Chemistry, Technology Review's Inaugural TR100 Young Innovator Award, American Institute of Chemical Engineers (AIChE) Allan P. Colburn Award, International Union of Biochemistry and Molecular Biology Jubilee Medal, Materials Research Society Fellowship, Royal Society of Chemistry Fellowship, Crown Prince Grand Prize in the Brunei Creative, Innovative Product and Technological Advancement (CIPTA) Award, American Institute for Medical and Biological Engineering Fellowship, Academy of Sciences of Iran Medal of Honor, American Association for the Advancement of Science Fellowship, and Singapore National Academy of Science Fellowship. Prof. Ying was elected a World Economic Forum Young Global Leader, and a member of the German National Academy of Sciences, Leopoldina. She was named one of the "One Hundred Engineers of the Modern Era" by AIChE in its Centennial Celebration. She was the inaugural winner of the Mustafa Prize "Top Scientific Achievement

Award" in 2015 for her research in bio-nanotechnology. She is the Editor-in-Chief of *Nano Today*.

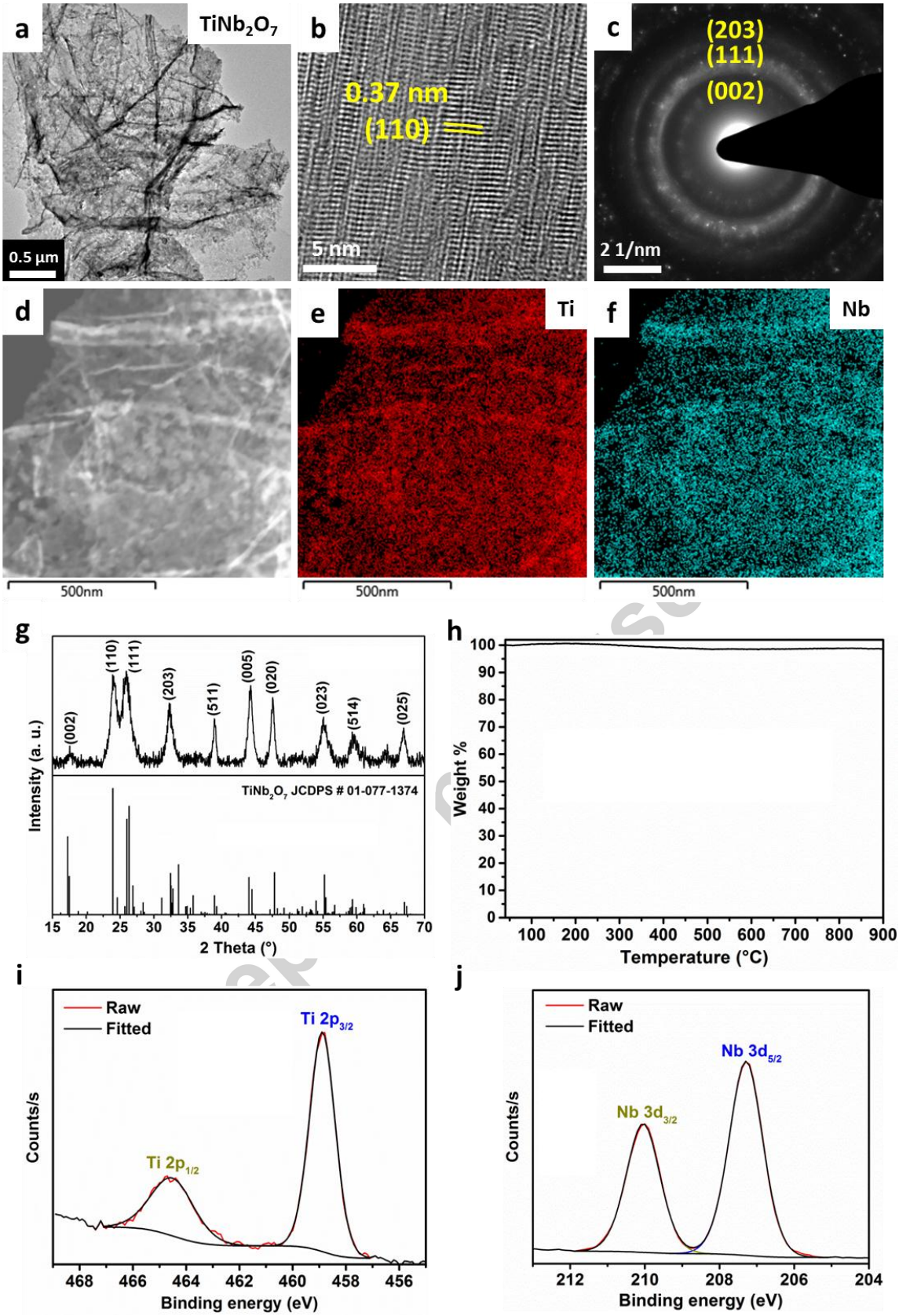

Figure 1. (a) TEM image, (b) HRTEM image, (c) SAED pattern, (d) STEM image, (e, f) EDX mapping images, (g) XRD pattern, (h) TGA profile, (i) XPS Ti 2p spectrum, and (j) XPS Nb 3d spectrum of $TiNb_2O_7$ nanosheets.

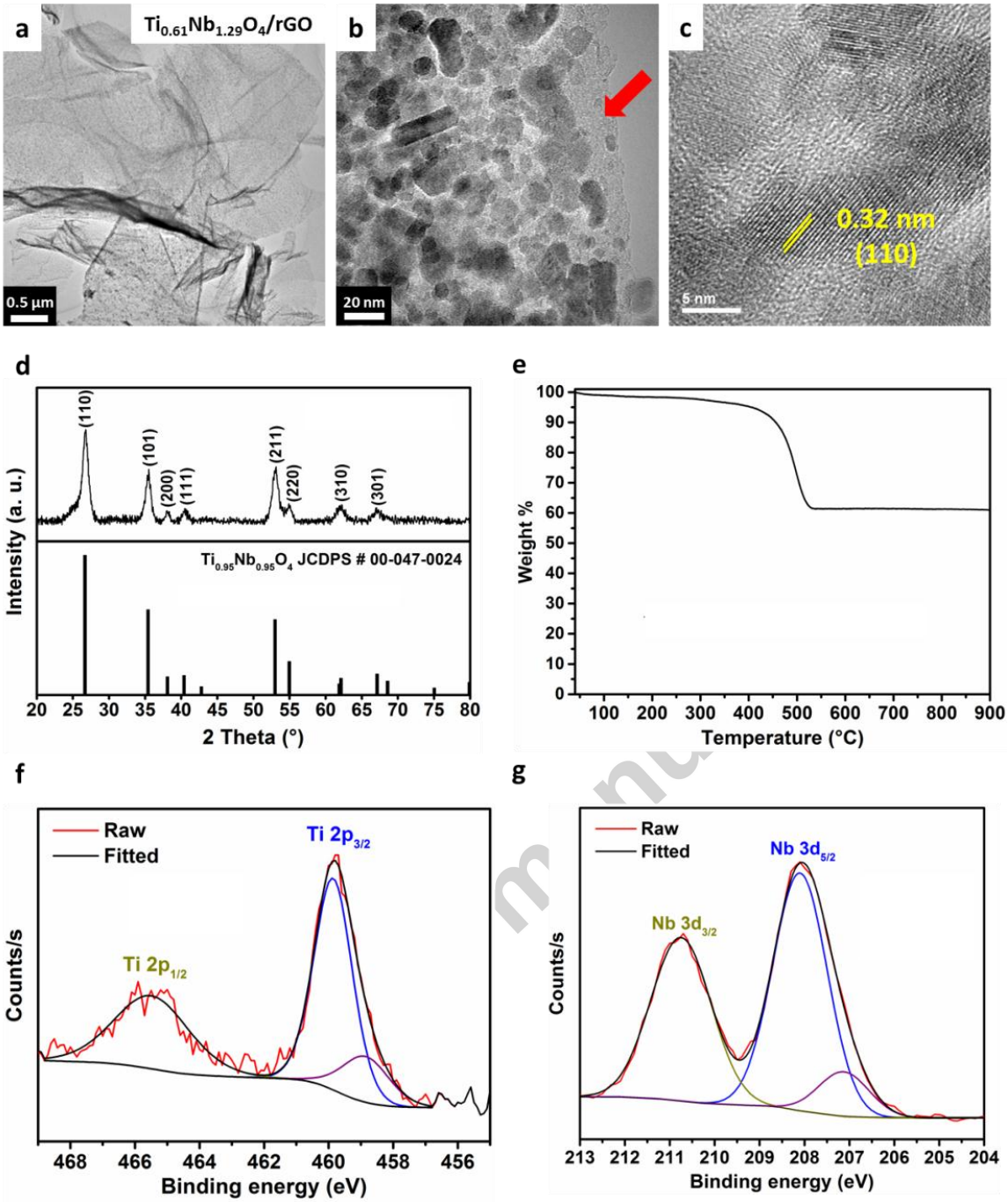

Figure 2. (a, b) TEM images, (c) HRTEM image, (d) XRD pattern, (e) TGA profile, (f) XPS Ti 2p spectrum, and (g) XPS Nb 3d spectrum of $Ti_{0.61}Nb_{1.29}O_4$/rGO nanosheets. Red arrow in (b) points to rGO sheet.

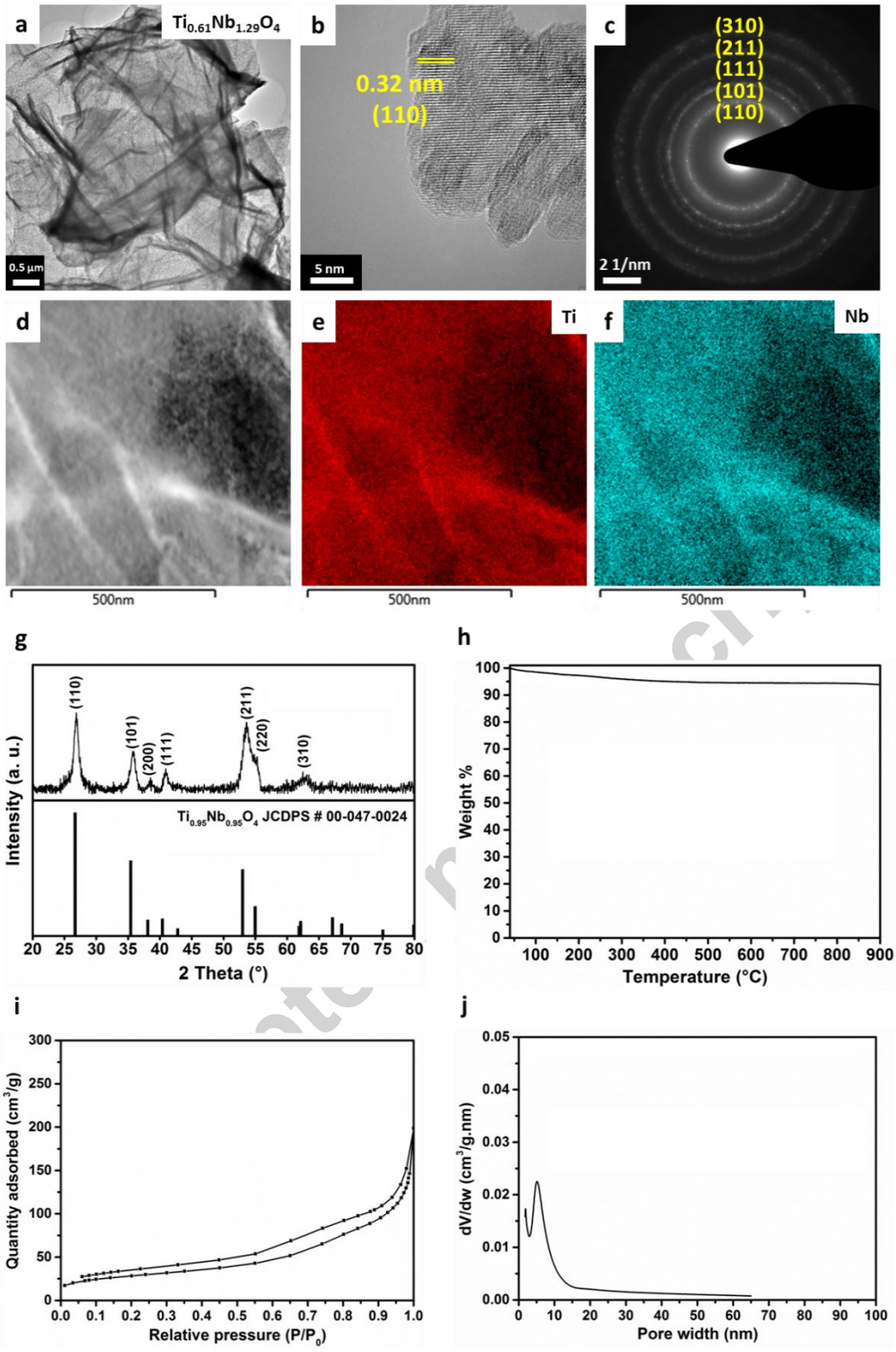

Figure 3. (a) TEM image, (b) HRTEM image, (c) SAED pattern, (d) STEM image, (e, f) EDX mapping images, (g) XRD pattern, (h) TGA profile, (i) nitrogen adsorption-desorption isotherm, and (j) pore size distribution of $Ti_{0.61}Nb_{1.29}O_4$ nanosheets.

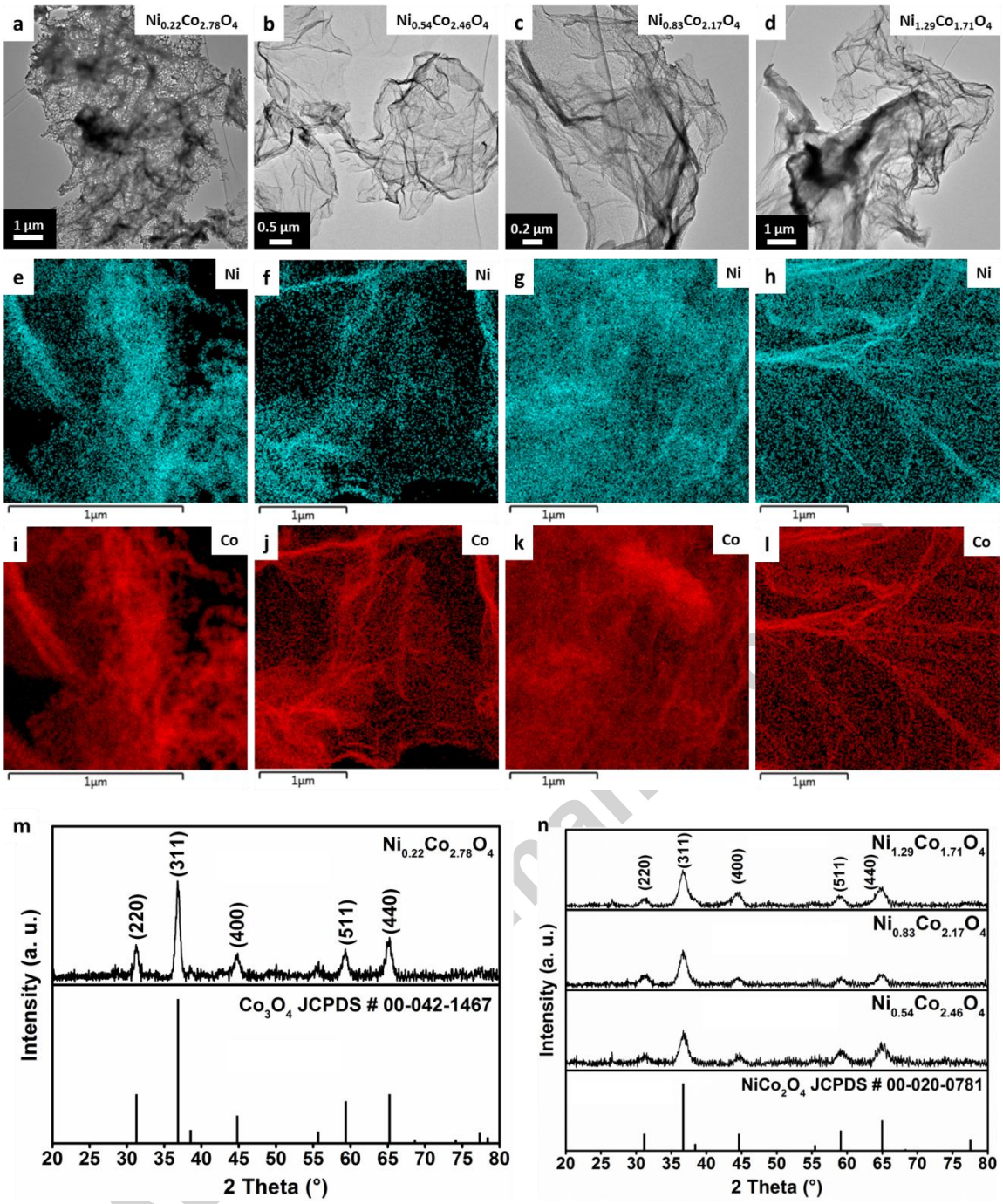

Figure 4. (a– d) TEM images, (e– l) EDX mapping images, and (m, n) XRD patterns of $Ni_xCo_{3-x}O_4$ nanosheets synthesized at 400 °C/1 h/air.

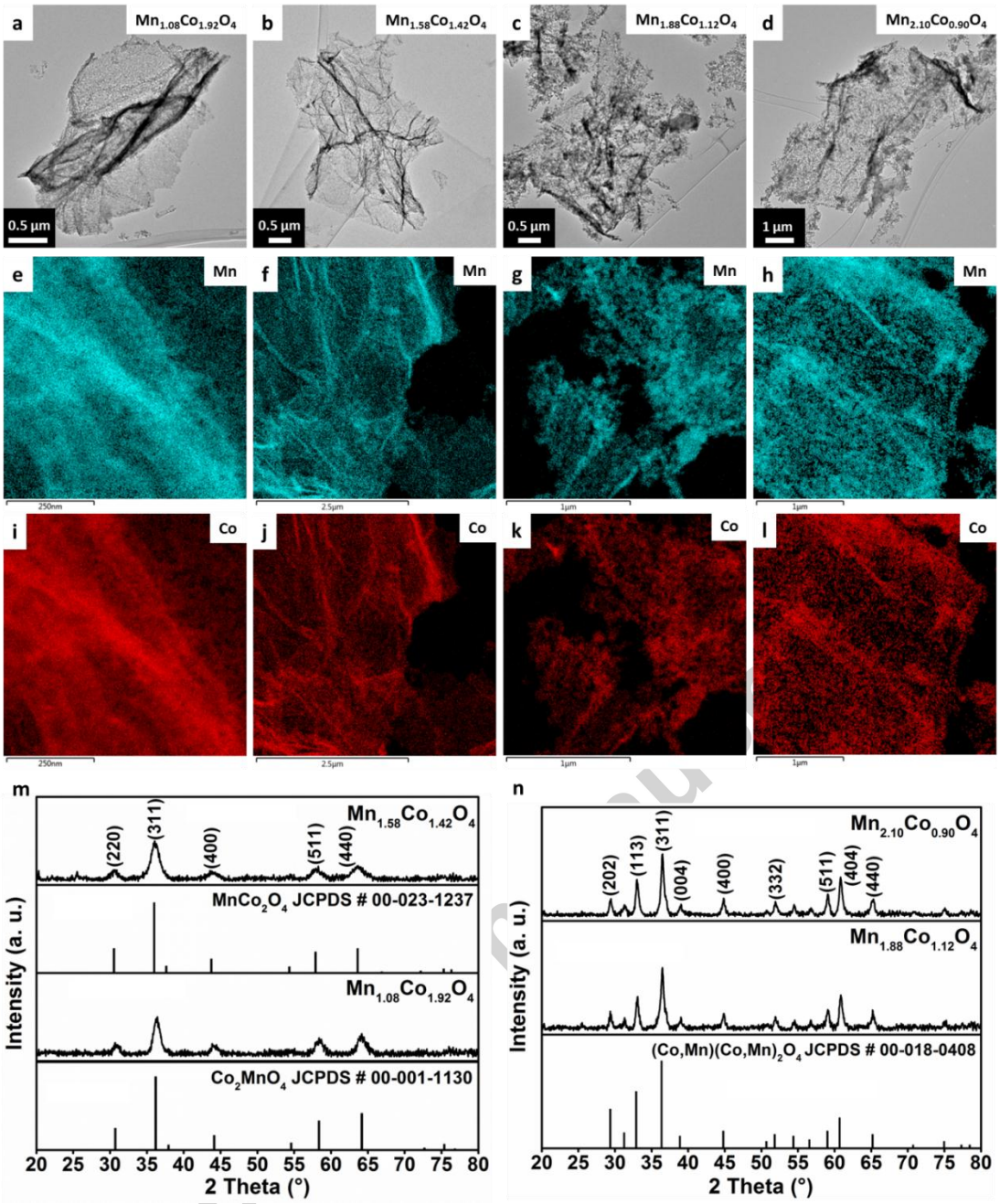

Figure 5. (a– d) TEM images, (e– l) EDX mapping images, and (m, n) XRD patterns of $Mn_xCo_{3-x}O_4$ nanosheets synthesized at 500 °C/1 h/air.

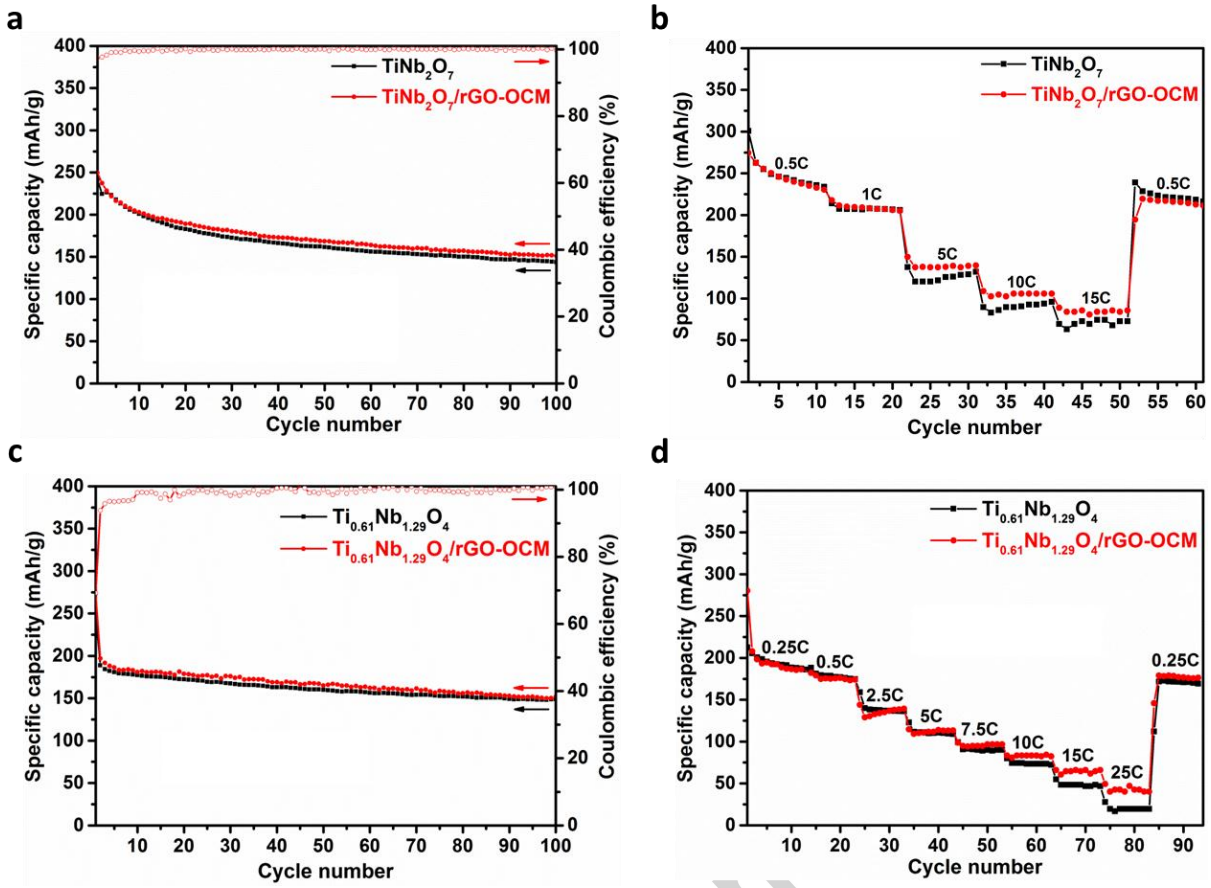

Figure 6. (a, c) Cycling and (b, d) rate performance of (a, b) $TiNb_2O_7$ and (c, d) $Ti_{0.61}Nb_{1.29}O_4$ nanosheets.

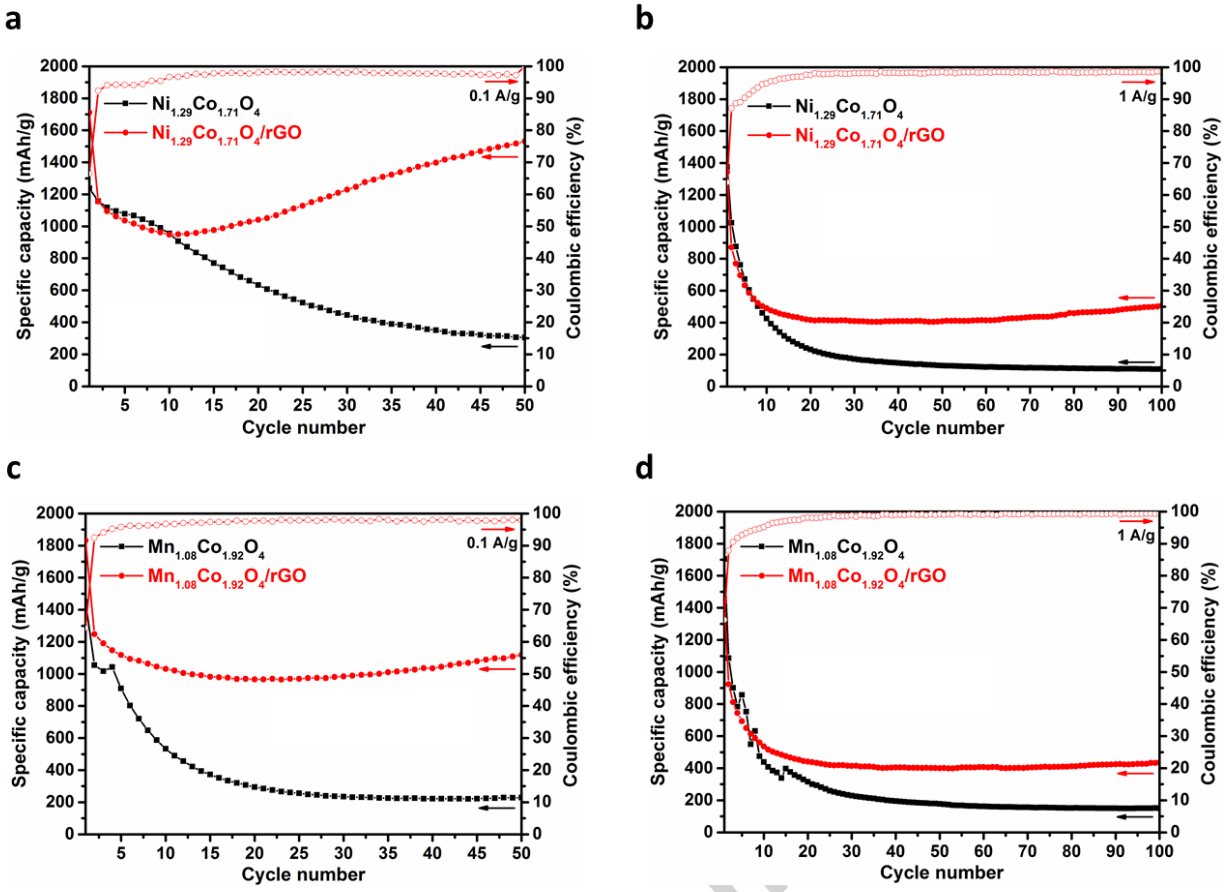

Figure 7. Cycling performance of (a, b) $Ni_{1.29}Co_{1.71}O_4$ and (c, d) $Mn_{1.08}Co_{1.92}O_4$ nanosheets at (a, c) 0.1 A/g and (b, d) 1 A/g.

Table 1. Synthesis conditions and properties of ternary oxide nanosheets.

Metal oxide	Precursors	Calcination conditions [a]	Crystal structure	Crystallite size (nm) [b]	rGO content (wt%)	BET specific surface area (m^2/g)
$TiNb_2O_7$	Ti(IV) butoxide Nb(V) ethoxide	700 °C/1 h	Monoclinic	14.9	0.0	23.8
$Ti_{0.61}Nb_{1.29}O_4$	Ti(IV) butoxide Nb(V) ethoxide	500 °C/1 h [c]	Tetragonal	8.0	0.0	98.7
$Ni_{1.29}Co_{1.71}O_4$/ rGO	Ni(II) + Co(II) acetylacetonate	325 °C/0.8 h	Cubic	4.2	31.3	85.9
$Ni_{1.29}Co_{1.71}O_4$	Ni(II) + Co(II) acetylacetonate	350 °C/1 h	Cubic	4.5	3.0	67.8
$Mn_{1.08}Co_{1.92}O_4$/ rGO	Mn(II) + Co(II) acetylacetonate	325 °C/0.3 h	Cubic	5.3	38.4	49.4
$Mn_{1.08}Co_{1.92}O_4$	Mn(II) + Co(II) acetylacetonate	500 °C/1 h	Cubic	6.8	2.9	41.5

[a]Calcination in air. [b]Based on (020) peak of $TiNb_2O_7$ and strongest peak of the other ternary oxide nanosheets. [c]Pre-calcined at 700 °C/2 h/Ar.

Research Highlights

- Nanosheets of ternary oxides have been successfully synthesized with graphene oxide planar-confined growth methodology
- $TiNb_2O_7$ and $Ti_{0.61}Nb_{1.29}O_4$ nanosheets are reported for the first time
- $Ni_xCo_{3-x}O_4$ and $Mn_xCo_{3-x}O_4$ nanosheets are derived with tunable compositions
- Ternary oxide nanosheets have been applied as Li-ion battery anodes with excellent performance

Graphical abstract